PCCP

PAPER

View Article Online
View Journal | View Issue

Cite this: *Phys. Chem. Chem. Phys.*, 2021, **23**, 24878

Oxygen-vacancy-induced magnetism in anti-perovskite topological Dirac semimetal Ba_3SnO

Javaria Batool,[ab] Syed Muhammad Alay-e-Abbas,*[ac] Gustav Johansson,[c] Waqas Zulfiqar,[a] Muhammad Arsam Danish,[a] Muhammad Bilal,[a] J. Andreas Larsson[c] and Nasir Amin[a]

The thermodynamic, structural, magnetic and electronic properties of the pristine and intrinsic vacancy-defect-containing topological Dirac semimetal Ba_3SnO are studied using first-principles density functional theory calculations. The thermodynamic stability of Ba_3SnO has been evaluated with reference to its competing binary phases Ba_2Sn, BaSn and BaO. Subsequently, valid limits of the atomic chemical potentials derived from the thermodynamic stability were used for assessing the formation of Ba, Sn and O vacancy defects in Ba_3SnO under different synthesis environments. Based on the calculated defect-formation energies, we find that the charge-neutral oxygen vacancies are the most favourable type of vacancy defect under most chemical environments. The calculated electronic properties of pristine Ba_3SnO show that inclusion of spin–orbit coupling in exchange–correlation potentials computed using generalized gradient approximation yields a semimetallic band structure exhibiting twin Dirac cones along the Γ–X path of the Brillouin zone. The effect of spin–polarization and spin–orbit coupling on the physical properties of intrinsic vacancy defects containing Ba_3SnO has been examined in detail. Using Bader charges, electron localization function (ELF), electronic density of states (DOS) and spin density, we show that the isolated oxygen vacancy is a magnetic defect in anti-perovskite Ba_3SnO. Our results show that the origin of magnetism in Ba_3SnO is the accumulation of unpaired charges at the oxygen vacancy sites, which couple strongly with the 5d states of the Ba atom. Owing to the metastability observed in earlier theoretically predicted magnetic topological semimetals, the present study reveals the important role of intrinsic vacancy defects in giving rise to magnetism and also provides opportunities for engineering the electronic structure of a Dirac semimetal.

Received 31st August 2021,
Accepted 18th October 2021

DOI: 10.1039/d1cp03989j

rsc.li/pccp

1. Introduction

Following the discovery of graphene, the Dirac equation has become highly relevant in solid-state physics for understanding the properties of materials that possess Dirac electrons in their electronic structure.[1,2] These so-called quantum materials exhibit nodal crossings in their electronic band structures, which cannot be explained solely on the basis of Landau theory.[3] Moreover, the non-trivial band topologies of these quantum materials remain invariant under topological transformations.[2–8] Thus, concepts from high-energy physics have not only enabled a better understanding of the physical properties such as magnetism and superconductivity of quantum materials but have also opened up new research avenues where device applications for these materials can be realized.[4,5] Depending on the presence of an insulating or semimetallic nature of the electronic structure in their bulk, we can classify these materials as topological insulators or topological semimetals, respectively. Although all topological materials have surface states, which are topologically protected by the crystal symmetry, the low-energy electrons in topological semimetals are quite interesting since they show very high mobilities due to the linear dispersion character of the corresponding electronic states.[9,10]

Since the competition between spin–orbit coupling (SOC) and band overlap in the presence of band inversion decides the classification of a topological material, inclusion of SOC in *ab initio* calculations often causes a band gap to appear in the electronic structure, giving us a topological crystalline insulator.[11,12] However, in some special cases the band overlap is much larger than the SOC,[12] such that a gapless band structure is obtained while the Dirac nodes are still protected by crystal symmetry. Realization of the robustness of the Dirac nodes against SOC leads to a topological Dirac semimetal (TDS), which is an attractive class

[a] *Computational Materials Modeling Laboratory, Department of Physics, Government College University Faisalabad, 38040 Faisalabad, Pakistan. E-mail: syed.muhammad.alay-e-abbas@ltu.se, alayabbas@gcuf.edu.pk*
[b] *Department of Physics, Government College Women University Faisalabad, Faisalabad, Pakistan*
[c] *Applied Physics, Division of Materials Science, Department of Engineering Sciences and Mathematics, Luleå University of Technology, 97187 Luleå, Sweden*

among a growing list of topological semimetals.[1] This is exactly the case in Ba_3SnO (BSO), which is unique among the Sn- and Pb-based A_3BO anti-perovskite materials and has been termed a prototypical example of a TDS.[12] Importantly, the simple cubic structure[13] and the presence of twin Dirac cones below the Fermi level in BSO[12] are interesting when compared with other TDSs like Cd_3As_2 or Na_3Bi[14–16] that adopt low-symmetry complex crystal structures. Consequently, large opportunities for modulating the electronic and magnetic properties of anti-perovskite BSO are available that can be realized by altering the crystal symmetry or chemical composition.

In recent years, interest in magnetic topological semimetals has considerably increased since in addition to exotic properties such as large thermoelectric currents and the intrinsic anomalous Hall effect, these materials also offer half-metallic features, which are a prerequisite for their utilization in spintronic devices.[1] The significance of both spin and charge degrees of freedom in phenomena such as the magneto-optic Kerr effect[17] and the magnon spin Nernst effect[18] has seen major discoveries made for low-dimensional materials where electronic and transport properties are influenced by SOC. For instance, transition metal trichalcogenides have gained much theoretical and experimental attention where magnetism in a 2D Dirac semimetal can be realized.[19–22] Although a number of magnetic Dirac semimetals have theoretically been proposed in the past,[23–25] their experimental synthesis is not generally viable owing to structural metastability and/or complex magnetic ordering. In this context, recent studies on anti-perovskites have clearly shown promising magnetic properties in their undoped forms, originating from the presence of intrinsic vacancy defects.[26–29] Magnetism arising from vacancy defects and related structural distortion[30–32] in undoped solids has become a focus of interest in recent years since the magnetic properties of these materials, especially oxides, can be easily tuned by varying the type and concentration of the vacancy defect. As metastability has so far posed serious challenges in the experimental realization of theoretically predicted magnetic topological semimetals,[23–25] in the present study we use first-principles density functional theory (DFT) calculations to show that charge-neutral intrinsic vacancy defects can induce stable magnetism in a TDS.

2. Computational details

The DFT calculations reported in the present work were performed using the all-electron augmented plane wave plus local orbitals (APW+lo) method available in the WIEN2k[33] computer program. By separating the crystal space into an interstitial region and non-overlapping muffin-tin spheres of radius 2.3 bohr, 2.0 bohr and 1.75 bohr for Ba, Sn and O, respectively, the wave functions inside these muffin-tin spheres were expanded using spherical harmonics where a maximum angular momentum (l_{max}) value of 10 was used. In the interstitial region, on the other hand, plane wave basis sets were utilized for which the charge density expansion vector (G_{max}) and the plane wave cut-off ($R_O K_{max}$) values of 18 $bohr^{-1}$ and 8, respectively, were used. For all the calculations reported in this work, an energy minimum of −7.0 Ry has been chosen to separate the core and valence states. The exchange–correlation potentials were modeled using the generalized gradient approximation (GGA) functional of Perdew, Burke and Ernzerhof (PBE).[34] The electron localization function was computed using the method proposed by Becke and Edgecombe.[35]

Since BSO is a topological material that contains heavy elements, the relaxed electronic structure reported in this work was computed using SOC that is included as a second variational method.[33] For the calculations involving the electronic structure of the bulk unit cell of BSO, an 11 × 11 × 11 *k*-mesh was used, which corresponds to 56 *k*-points in the irreducible wedge of the first Brillouin zone. On the other hand, the electronic structures of the vacancy containing 2 × 2 × 2 supercells of BSO were simulated using a 5 × 5 × 5 *k*-mesh. For the termination of the self-consistent field cycles the energy and charge convergence criteria were set to 10^{-5} Ry and 10^{-4} *e*, respectively, while forces on atomic species appearing as a result of introducing vacancy defects in the supercell were minimized to a value below 1 mRy $a.u.^{-1}$. To construct the vacancy-containing supercells of BSO, we first optimized the lattice parameter of the bulk unit cell of BSO by fitting the total energy *vs.* the unit cell volume data to the Murnaghan equation of state.[36] The calculated lattice parameter of BSO (Table 1) is in good agreement with the room-temperature lattice parameters reported in experimental studies for BSO.[13,37] Using the optimized unit cell, we constructed a 2 × 2 × 2 supercell containing 40-atoms to simulate the charge-neutral Ba, Sn and O vacancies in BSO. Introduction of the three intrinsic vacancies V_Z^0 (where Z = Ba, Sn or O) in BSO using the 2 × 2 × 2 supercells yielded chemical compositions of $Ba_{23}Sn_8O_8$, $Ba_{24}Sn_7O_8$ and $Ba_{24}Sn_8O_7$, corresponding to a 4.167% Ba vacancy concentration, a 12.5% Sn vacancy concentration and a 12.5% O vacancy concentration. All the vacancy-containing supercells of BSO were geometrically optimized to eliminate residual atomic forces. Subsequently, spin-polarized (SP) calculations with different magnetic ordering

Table 1 GGA-calculated lattice parameters of Ba_3SnO, Ba_2Sn, BaSn, BaO, Ba and Sn compared with experimental data and earlier theoretical studies

	Lattice parameters (Å)		
System (space group)	Present work	Other theoretical	Experimental
Ba_3SnO (# 221: $Pm\bar{3}m$)			
a_0	5.509	5.526[40]	5.448[13]
Ba_2Sn (# 62: *Pnma*)			
a_0	8.792	8.841[40]	8.615[43]
b_0	5.630	5.687[40]	5.690[43]
c_0	10.786	10.750[40]	10.078[43]
BaSn (# 63: *Cmcm*)			
a_0	5.362	5.374[40]	5.316[44]
b_0	12.660	12.776[40]	12.550[44]
c_0	4.698	4.725[40]	4.657[44]
BaO (# 225: $Fm\bar{3}m$)			
a_0	5.593	5.615[40]	5.546[45]
Ba (# 229: $Im\bar{3}m$)			
a_0	5.017	5.030[40]	5.020[46]
Sn (# 227: $Fd\bar{3}m$)			
a_0	6.647	6.646[40]	6.481[47]

were performed to examine the stability of the magnetism introduced by the presence of the intrinsic vacancies.

3. Results and discussion

3.1. Structural properties and thermodynamic stability of pristine Ba_3SnO

Table 1 presents the GGA-calculated lattice parameters of BSO where one can see good agreement with previous theoretical and experimental data. In the cubic anti-perovskite unit cell of BSO, the Sn atoms occupy the corner Wyckoff position 2a (*i.e.* (0, 0, 0)) of the $Pm\bar{3}m$ structure, while the Ba and O atoms are located at the face-centered 6b (*i.e.* (1/2, 1/2, 0), (1/2, 0, 1/2) and (0, 1/2, 1/2)) and body-centered 2a (*i.e.* (1/2, 1/2, 1/2)) Wyckoff positions, respectively.[13] This is contrary to the case of normal cubic ABO_3 perovskite oxides such as $SrTiO_3$ and $BaZrO_3$, where the A, B and O atoms occupy 2a corner, 2a body-centered and 6b face-centered Wyckoff positions, respectively.[38] Consequently, in anti-perovskite BSO an O atom is coordinated octahedrally with six Ba atoms to form a Ba_6O octahedron, while a Sn atom is coordinated cuboctahedrally with twelve Ba atoms. For the GGA-optimized unit cell of BSO, we find that all the Ba–O distances within the Ba_6O octahedron are 2.754 Å and the cuboctahedrally coordinated Ba–Sn distances are 3.895 Å. Since the thermodynamic stability of BSO requires its enthalpy of formation (*i.e.*, $\Delta_f H_{Ba_3SnO}$) to be more negative than the cumulative enthalpies of other Ba-based chemical systems,[39,40] we have also optimized the lattice parameters of relevant solid phases that compete with the synthesis of BSO. Comparison of our calculated structural properties for Ba_2Sn, BaSn, BaO, Ba and Sn (Table 1) with experimental data shows the usual overestimation by GGA functionals. However, it is evident that our APW+lo-based results are in better agreement with experimental data compared with previous DFT calculations performed using the projector augmented-wave method.[40] Using the ground-state lattice parameters of BSO, Ba_2Sn, BaSn, BaO, Ba and Sn presented in Table 1, the minimum total energies were computed, which are represented by $E^t_{Ba_3SnO}$, $E^t_{Ba_2Sn}$, E^t_{BaSn}, E^t_{BaO}, E^t_{Ba} and E^t_{Sn}, respectively.[40] For the case of an oxygen molecule, on the other hand, the total energy $\left(E^t_{O_2}\right)$ was computed by adding the ground-state energy of an isolated oxygen atom[41] to the GGA cohesive energy of the oxygen molecule reported in ref. 42.

For the four Ba-based binary and ternary compounds listed in Table 1, we can define the enthalpies of formation as the differences in the DFT-calculated total energies of the compounds and their constituent elemental species in their standard reference states.[48] Using the formulas

$$\Delta_f H_{Ba_3SnO} = E^t_{Ba_3SnO} - 3E^t_{Ba} - E^t_{Sn} - \frac{1}{2}E^t_{O_2} \quad (1)$$

$$\Delta_f H_{Ba_2Sn} = E^t_{Ba_2Sn} - 2E^t_{Ba} - E^t_{Sn} \quad (2)$$

$$\Delta_f H_{BaSn} = E^t_{BaSn} - E^t_{Ba} - E^t_{Sn} \quad (3)$$

Table 2 Calculated enthalpies of formation (in eV f.u.$^{-1}$) for Ba_3SnO, Ba_2Sn, BaSn and BaO along with available experimental and theoretical data. For the sake of completeness, the calculated cohesive energies (in eV per atom) of Ba and Sn are also provided

	Enthalpy of formation (eV f.u.$^{-1}$)		
Compounds	Present work	Other theoretical	Experimental
Ba_3SnO	−7.448	−7.675[40]	—
Ba_2Sn	−1.867	−1.824[40]	−3.514[a],[50] −3.887[b] [51]
BaSn	−1.425	−1.407[40]	−1.136[c] [52]
BaO	−5.387	−5.662[40]	−5.680[53]

	Cohesive energies (eV per atom)		
Bulk elements	Present work	Other theoretical	Experimental
Ba	−1.814	−1.886[49]	−1.897[54]
Sn	−3.167	−3.171[49]	−3.140[54]

[a] $Ba_{0.67}Sn_{0.33}$ alloy between 696 K and 948 K from ref. 50. [b] Ba_2Sn at 843 K from ref. 51. [c] $Ba_{0.56}Sn_{0.44}$ at 1300 K from ref. 52.

and

$$\Delta_f H_{BaO} = E^t_{BaO} - E^t_{Ba} - \frac{1}{2}E^t_{O_2} \quad (4)$$

we computed the enthalpies of formation of BSO, Ba_2Sn, BaSn and BaO, respectively, which are presented in Table 2. It is evident from Table 2 that the calculated value of the enthalpy of formation for BaO compares well with the experimental data. On the other hand, the enthalpies of formation computed for Ba_2Sn and BaSn are found to be significantly different from the high-temperature values reported in experiments.[50–52] The deviation of the theoretically calculated enthalpies of formation for Ba_2Sn and BaSn from high-temperature experimental data was also observed in previous DFT studies.[40] Although our calculated $\Delta_f H_{Ba_3SnO}$ compares well with previous theoretical results,[40] no experimental data for BSO are available in the literature for comparison, to the best our knowledge. Because our DFT enthalpy of formation for BaO and the cohesive energies of Ba and Sn are in good agreement with experimental values,[53,54] further experimental efforts for determining the standard enthalpies of formation of Ba_2Sn, BaSn and BSO at lower temperatures are still needed. For the case of BSO it is interesting to note that the large negative enthalpy of formation (around −750 kJ mol^{-1}) indicates that this compound may be obtained from pure elemental phases Ba, Sn and O_2 through a one-step synthesis method.[55] Moreover, the sum of our calculated values $\Delta_f H_{Ba_2Sn}$ and $\Delta_f H_{BaO}$ is less negative than $\Delta_f H_{Ba_3SnO}$, suggesting that cubic BSO can also be synthesized using a two-step synthesis method having a chemical equation of $Ba_2Sn + BaO \rightarrow Ba_3SnO$.

In order to establish the chemical stability of BSO, the thermodynamic stability diagram of this compound was computed in terms of the atomic chemical potentials of Ba, Sn and O.[39,56,57] For this reason, we first define the atomic chemical potentials of Ba, Sn and O in their stable reference states as $\mu^{solid}_{Ba} = E^t_{Ba}$, $\mu^{solid}_{Sn} = E^t_{Sn}$ and $\mu^{gas}_{O} = 1/2E^t_{O_2}$. Based on these definitions, the atomic chemical potentials of Ba, Sn and O in BSO should be written as $\mu_{Ba} = \mu^{solid}_{Ba} + \Delta\mu_{Ba}$, $\mu_{Sn} = \mu^{solid}_{Sn} + \Delta\mu_{Sn}$

and $\mu_O = \mu_O^{gas} + \Delta\mu_O$, where $\Delta\mu_{Ba}$, $\Delta\mu_{Sn}$ and $\Delta\mu_O$ are the allowed variations in the chemical potentials of their stable reference states. This, therefore, allows us to rewrite eqn (1) as

$$\Delta_f H_{Ba_3SnO} = 3\Delta\mu_{Ba} + \Delta\mu_{Sn} + \Delta\mu_O. \quad (5)$$

It is important to note here that the allowed variations in the atomic chemical potentials should satisfy $\Delta\mu_{Ba} \leq 0$, $\Delta\mu_{Sn} \leq 0$ and $\Delta\mu_O \leq 0$ in order to allow the thermodynamically stable formation of BSO. Moreover, in order to eliminate the precipitation of binary phases Ba_2Sn, BaSn and BaO, $\Delta\mu_{Ba}$, $\Delta\mu_{Sn}$ and $\Delta\mu_O$ used in eqn (5) must also satisfy[58]

$$\Delta_f H_{Ba_2Sn} \geq 2\Delta\mu_{Ba} + \Delta\mu_{Sn} \quad (6)$$

$$\Delta_f H_{BaSn} \geq \Delta\mu_{Ba} + \Delta\mu_{Sn} \quad (7)$$

$$\Delta_f H_{BaO} \geq \Delta\mu_{Ba} + \Delta\mu_O \quad (8)$$

From the above expressions, we can now identify two points, A and F, in a two-dimensional $\Delta\mu_{Ba}-\Delta\mu_{Sn}$ plane where

$$\text{Point A: } \Delta_f H_{Ba_3SnO} = 3\Delta\mu_{Ba} + \Delta\mu_{Sn} + \Delta\mu_O, \quad \Delta_f H_{BaO} = \Delta\mu_{Ba} + \Delta\mu_O \text{ and } \Delta\mu_{Ba} = 0 \quad (9)$$

$$\text{Point F: } \Delta_f H_{Ba_3SnO} = 3\Delta\mu_{Ba} + \Delta\mu_{Sn} + \Delta\mu_O, \quad \Delta_f H_{BaO} = \Delta\mu_{Ba} + \Delta\mu_O \text{ and } \Delta\mu_{Sn} = 0 \quad (10)$$

which correspond to the extreme values of valid variations in the atomic chemical potentials where BSO can be synthesized in competition with BaO, Ba and Sn. Similarly, points B and E for BSO within the $\Delta\mu_{Ba}-\Delta\mu_{Sn}$ plane can be defined as

$$\text{Point B: } \Delta_f H_{Ba_3SnO} = 3\Delta\mu_{Ba} + \Delta\mu_{Sn} + \Delta\mu_O, \quad \Delta_f H_{Ba_2Sn} = 2\Delta\mu_{Ba} + \Delta\mu_{Sn} \text{ and } \Delta\mu_{Ba} = 0 \quad (11)$$

$$\text{Point E: } \Delta_f H_{Ba_3SnO} = 3\Delta\mu_{Ba} + \Delta\mu_{Sn} + \Delta\mu_O, \quad \Delta_f H_{Ba_2Sn} = 2\Delta\mu_{Ba} + \Delta\mu_{Sn} \text{ and } \Delta\mu_{Sn} = 0 \quad (12)$$

which restrict the formation of the competing Ba_2Sn, Ba and Sn phases. Although all values of $\Delta\mu_{Sn}$ and $\Delta\mu_{Ba}$ within the region enclosed by the points A, B, E and F satisfy eqn (5), it is evident that eqn (7) is not satisfied at points E and F. Since this could result in the precipitation of BaSn, restricting the synthesis of BSO, we further define two points C and D as

$$\text{Point C: } \Delta_f H_{Ba_3SnO} = 3\Delta\mu_{Ba} + \Delta\mu_{Sn} + \Delta\mu_O, \quad \Delta_f H_{Ba_2Sn} = 2\Delta\mu_{Ba} + \Delta\mu_{Sn} \text{ and } \Delta_f H_{BaSn} \geq \Delta\mu_{Ba} + \Delta\mu_{Sn} \quad (13)$$

$$\text{Point D: } \Delta_f H_{Ba_3SnO} = 3\Delta\mu_{Ba} + \Delta\mu_{Sn} + \Delta\mu_O, \quad \Delta_f H_{BaO} = \Delta\mu_{Ba} + \Delta\mu_O \text{ and } \Delta_f H_{BaSn} \geq \Delta\mu_{Ba} + \Delta\mu_{Sn}, \quad (14)$$

where BSO can exist stably with respect to all binary compounds of barium as well as the elemental phases Ba and Sn.

The thermodynamic stability diagram of BSO within the $\Delta\mu_{Ba}-\Delta\mu_{Sn}$ plane is shown in Fig. 1, where all the stability points defined in eqn (9)–(14) are shown. In Fig. 1, the light gray area enclosed by points A, B, C and D represents the thermodynamic stability region of BSO where it can be formed

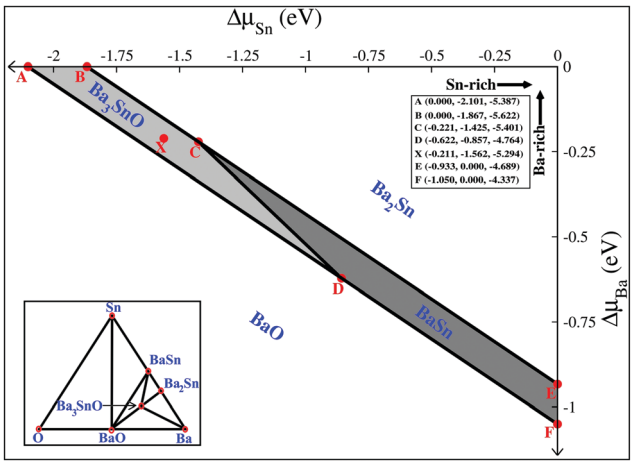

Fig. 1 Calculated thermodynamic stability region of Ba_3SnO (light gray area) enclosed by the points A, B, C and D in terms of the atomic chemical potentials of Ba and Sn. The inset at the top right corner shows the DFT-calculated values of the chemical potential variation for the points shown as red dots on the thermodynamic stability diagram, while the inset in the lower left corner shows the compositional ternary plot for the compounds competing with the synthesis of Ba_3SnO.

with respect to the binary competing phases Ba_2Sn, BaSn and BaO.[58] An additional point X in the middle of the stability diagram corresponds to the center of BSO's stability region, which gives us a nominal chemical environment where this anti-perovskite can be obtained without the possibility of the precipitation of any of the competing phases containing Ba or Sn. It is clear from Fig. 1 that the inclusion of BaSn in the thermodynamic stability diagram of BSO has significantly reduced its stability region. As a result, the $\Delta\mu_{Sn} = 0$ and $\Delta\mu_O = 0$ chemical environments are not allowed during the synthesis of BSO. This can be attributed to the larger proportion of barium in BSO, which can be better understood from the compositional triangular plot shown as the lower left inset in Fig. 1. It is clear from the triangular inset in Fig. 1 that the successful synthesis of BSO can be realized near the maximum Ba composition point, which corresponds to the Ba-rich (*i.e.*, $\Delta\mu_{Ba} = 0$) chemical environment in the thermodynamic stability diagram. At the same time, the inset in Fig. 1 also indicates that the binary oxides of tin will not restrict the stability region of BSO. In order to test this assumption, we also computed the enthalpies of formation for SnO (space group # 129: *P*4/*nmm*) and SnO_2 (space group # 136: *P*42/*mnm*) using their structurally optimized unit cells, which are found to be $\Delta_f H_{SnO} = -2.872$ eV f.u.$^{-1}$ and $\Delta_f H_{SnO_2} = -5.518$ eV f.u.$^{-1}$. Similar to the case of BaO, the GGA-calculated enthalpies of formation for SnO and SnO_2 are slightly underestimated compared with the experimental values of -2.962 eV f.u.$^{-1}$ and -6.021 eV f.u.$^{-1}$,[59] respectively. However, since $\Delta_f H_{SnO} > \Delta\mu_{Sn} + \Delta\mu_O$ and $\Delta_f H_{SnO_2} > \Delta\mu_{Sn} + 2\Delta\mu_O$ for all the stability points defined in eqn (9)–(14), it is evident that SnO and SnO_2 do not have any influence on the stability region enclosed by points A, B, C and D (Fig. 1). Fig. 1 also shows that BSO can be obtained by varying $\Delta\mu_{Ba}$ from 0 eV (point A or point B) to

-0.622 eV (point D), while $\Delta\mu_{Sn}$ can be varied from -0.857 eV (point D) to -2.101 eV (point A). Based on this situation we can designate both point A and point B as the allowed Ba-rich chemical environments for BSO, while point D can be designated as a Ba-poor chemical environment. Since the variation of $\Delta\mu_O$ within the stability region of BSO is from -4.767 eV to -5.622 eV, point D and point B in Fig. 1 correspond to extreme oxidation (O-rich) and reduction (O-poor) conditions allowed for the stable synthesis of BSO, respectively.

3.2. Electronic properties of pristine Ba_3SnO

Like other members of the tin- and lead-containing anti-perovskite oxides, the electronic properties of BSO are sensitive to SOC interactions.[12,28,60] Judging from the electron precise octet rule for an oxide having a chemical composition of $Ba_3^{2+}Sn^{4-}O^{2-}$, one would expect a band gap to appear between the cation and anion states around the Fermi level. However, this is not the case for topological materials since their electronic structures are strongly influenced by competition between the crystal symmetry, SOC and band overlap. Earlier DFT studies based on GGA as well as hybrid DFT calculations have shown that BSO has a significantly larger band overlap compared with Ca_3SnO (CSO) and Sr_3SnO (SSO);[12] the Ba-5d and Sn-5p states contribute significantly both above and below the Fermi level even, with the inclusion of SOC. In order to elucidate on the effect of SOC on BSO's electronic properties, in the present work we compare the electronic band structure diagrams of BSO without (Fig. 2(a)) and with (Fig. 2(b)) the inclusion of SOC. Since the semimetallic Dirac cones in BSO emerge away from the Γ symmetry point, the band structures were computed for k-paths corresponding to the bulk (R–Γ–X–M–Γ) as well as their projection along the (001) surface (M–Γ–X) of the anti-perovskite structure.

When SOC is not taken into consideration, the electronic properties of BSO computed using the GGA functional show a semimetallic nature along with a single Dirac cone appearing below the Fermi level along the Γ–X path. From the fat-band representation shown in Fig. 2(a), it is clear that the electronic bands appearing just above the Fermi level in bulk BSO near the Γ point have a Sn-5p character that persists when this band moves to negative energy values along the Γ–X path. When the SOC interactions are taken into account (Fig. 2(b)), the electronic band along the Γ–X path is split into two branches; the Sn-5p character still persists and twin Dirac cones appear

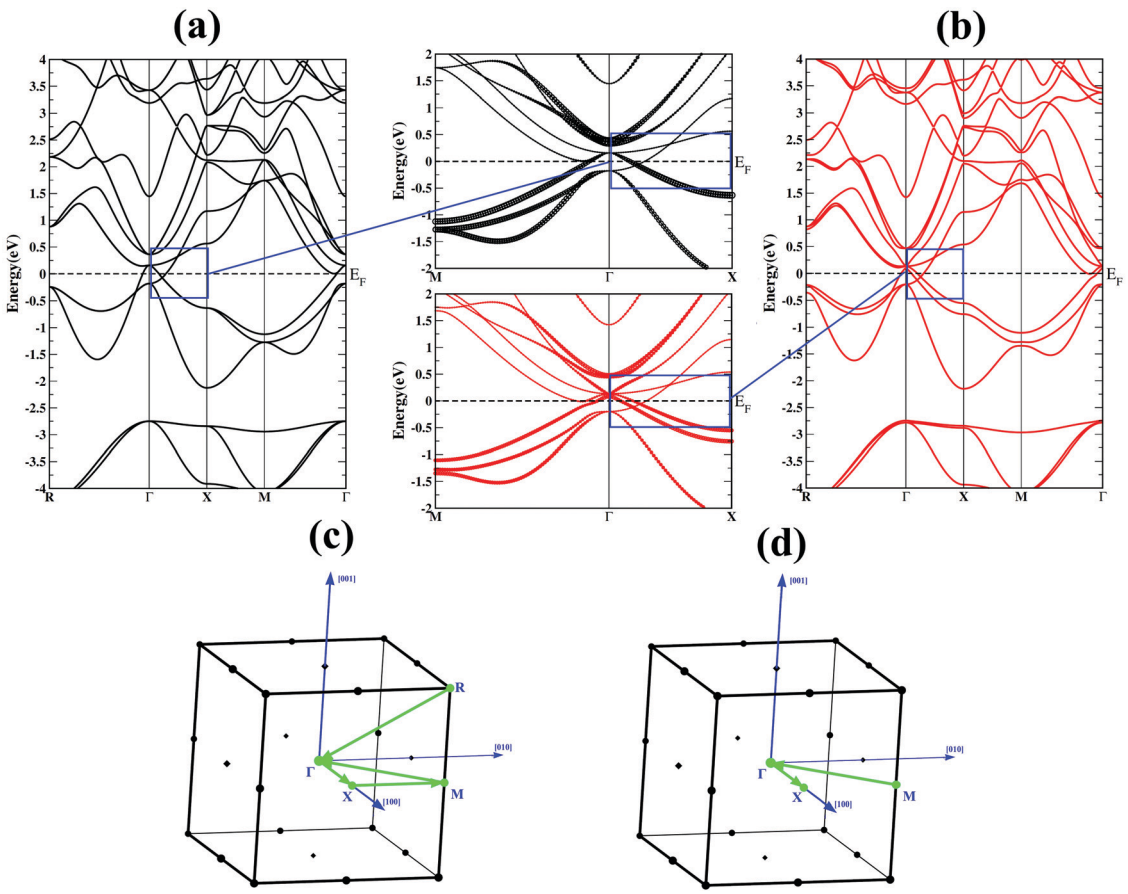

Fig. 2 Electronic band structure diagrams of Ba_3SnO computed (a) without and (b) with the inclusion of SOC. The band structures are computed along the (c) R–Γ–X–M–Γ and (d) M–Γ–X k-paths to capture the behaviour of the electronic bands in the bulk Brillouin zones and their projection along the (001) surface. For comparing the effect of SOC on bands along the M–Γ and Γ–X k-paths of the (001) surface, fat-band representation is used where the size of symbol indicates the contribution of the Sn-5p states.

below the Fermi level. This clearly shows the robustness of the Dirac cones of BSO in the presence of SOC, which may provide opportunities for band engineering this semimetal.[61] It is also interesting to note that a small splitting of the bands along the R–Γ (M–Γ) path of the bulk (surface) Brillouin zone is also achieved in both the conduction and valence bands. Our calculated band structures are in good agreement with those of recent studies carried out using the GGA parameterization scheme;[12] however, the magnitude of the band splitting along the R–Γ (as well as the M–Γ) k-path is slightly smaller than the that computed using msBJLDA.[62] It is worth pointing out here that despite the variations in the size of the overlap obtained using different DFT functionals,[58] earlier DFT studies performed using GGA,[12,63] HSE,[12] and mBJLDA[62] as well as a tight-binding model[62] also showed twin Dirac cones for this semimetal appearing along the Γ–X k-path.[63] Finally, comparison of the electronic band structures shown in Fig. 2 with topological insulators like CSO[28] and Ca_3PbO (CPO)[11] also confirms the twin Dirac cones and the TDS nature of this compound.

To further explore the contribution of different electronic states of Ba, Sn and O in the electronic band structure of BSO around the Fermi level, we computed the total density of states (TDOS) and projected density of states (PDOS) for BSO, which are shown in Fig. 3. A comparison of the plots shown in Fig. 3 also confirms a weaker SOC in BSO, which results in only slight changes in the overall DOS profiles. It is also evident that for calculations performed both without and with the inclusion of SOC, the TDOS at the Fermi level is non-zero, indicating a mixing of the cation and anion states at the Fermi level that results in a semimetallic band structure. Irrespective of the inclusion of SOC, Fig. 3 reveals that the upper valence band of BSO is mainly composed of Sn-5p states with a minor contribution coming from Ba-5d states. Within the −2 eV to −5 eV energy range, on the other hand, the contribution of O-2p states dominates the PDOS. It is interesting to note that within this energy region, the Ba-5d states have a more pronounced contribution compared with the Sn-5p states. From the conduction band PDOS of BSO shown in Fig. 3, it is clear that the Ba-5d states dominate the energy bands located above the Fermi level. Interestingly, the second prominent contribution above the Fermi level is due to Sn-5p states, while the contribution of the Ba-6s states is negligible. Overall, in the vicinity of the Fermi level an inverted contribution of the Ba-5d and Sn-5p states in the valence and conduction bands, respectively, is evident, confirming the band overlap observed in Fig. 2.

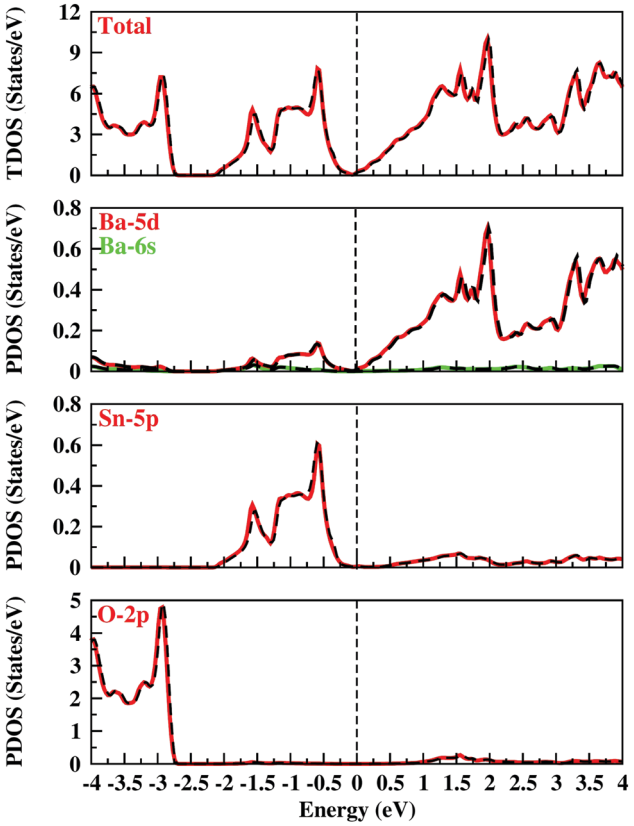

Fig. 3 Calculated total density of states (TDOS) together with the projected density of states (PDOS) of Ba_3SnO showing the contribution of the Ba-6s, Ba-5d, Sn-5p and O-2p states to bands located in the energy window of −4 eV to 4 eV around the Fermi level. Results computed without (black dashed lines) and with (red solid lines) the inclusion of SOC are shown.

3.3. Metallic bonding and ionic binding properties of pristine Ba_3SnO

For the whole PDOS energy range shown in Fig. 3, one cannot see any contribution of Ba-6s states in either the conduction or valence band states of BSO. This clearly indicates the departure of Ba from its usual electronic configuration (*i.e.*, $[Xe]5d^06s^2$) according to the aufbau principle to become $[Xe]5d^26s^0$ in BSO by both promoting electrons from Ba-6s to Ba-5d states and loss of electrons due to the +2 oxidation state (see the computed partial charges below). Since these electrons are subsequently predominantly donated to the surrounding Sn^{4-} and O^{2-} anions to form ionic binding, we can see the dominance of the Ba-5d, Sn-5p and O-2p states around the Fermi level. In order to obtain a quantitative assessment of the ionic nature between the cations and anions in pristine BSO, we computed the Bader charges[64] for Ba, Sn and O atoms, which are found to be 1.146 e (1.149 e), −1.990 (−1.998 e) and −1.442 e (−1.442 e), respectively, from calculations performed with (without) the inclusion of SOC. It is clear that SOC brings about a small change in the effective Bader charges of only Ba and Sn atoms, which is in accordance with the small variation observed in the DOS plots upon introducing SOC.

Earlier theoretical studies of anti-perovskites like CSO, SRO and CPO[11] have frequently shown that a smaller band overlap of the A atom's d states and the B atom's p states is responsible for their topological crystalline insulator classification[11] compared with the semimetallic BSO.[12] Although the electronic properties presented in Fig. 2 and 3 confirm the semimetallic nature of BSO, it is intuitive to compare the differences in the bonding properties of A_3BO anti-perovskites to elucidate further the differences in their electronic structures. This is particularly important in view of the fact that the polar layered perovskite-like structures (made up of $[AB]^{2-}$ and $[A_2O]^{2+}$ layers

in the A_3BO anti-perovskite along, *e.g.*, the [001] direction) give rise to unusual physical and chemical properties.[65,66] The proximity of the calculated Bader charges to the charge states of Ba^{2+}, Sn^{4-} and O^{2-} already shows that the Ba···O binding is more ionic in nature compared with the Ba···Sn binding. On the other hand, comparison of the Bader charges for BSO with the those reported for Ca (1.302 *e*), Sn (−2.380 *e*) and O (−1.542 *e*) in CSO at the PBE GGA level[28] clearly indicates the difference in the binding character within the AB and A_2O layers of CSO and BSO. Therefore, the binding properties inside and among the AB and A_2O layers might be responsible for the size of the band overlap that results in the insulating and semimetallic character of the band structure. Since the binary competing phases CaSn and BaSn of CSO and BSO, respectively, are already known to be metallic in nature,[52,67] it can further be inferred that the degree of metallic bonding in the AB layer of A_3BO anti-perovskites should relate to the size of the band overlap. In order to examine the role of metallic bonding on the size of overlap within the AB and A_2O layers of CSO and BSO, we computed the electron localization functions (ELFs) for these two compounds, which are presented in Fig. 4(a and b). As the ELF values can be directly linked with the metallic bonding,[68,69] the ELF profiles of the metallic interaction between the Sn atoms in CSO and BSO are also shown in Fig. 4(c). It is clear from Fig. 4(a and b) that the A···Sn and A···O binding in both CSO and BSO is ionic (no chemical bonding is present). Moreover, larger ELF values at the Ca and O sites for CSO confirm a relatively stronger ionic binding evident from the Bader charges. Although both the CaSn layer of CSO and the BaSn layer of BSO show metallic bonding (*i.e.*, 0.7 < ELF value < 0.2) between the Sn atoms,[68] it is interesting to note from the ELF profiles (Fig. 4(c)) that midway between the two Sn atoms in an AB layer and two Ca/Ba atoms in an A_2O layer the metallic bonding between the Sn atoms in CSO is slightly larger. This indicates that the smaller interaction between the two Sn atoms in BSO results in a larger contribution of the Sn-5p states above the Fermi level. As a consequence, a larger band overlap is observed in BSO, which is responsible for giving this material a semimetallic band structure.

3.4. Formation energies of vacancy defects in Ba_3SnO

Vacancy defects play a crucial role in determining the physical properties of solid-state materials. As mentioned earlier, non-stoichiometric anti-perovskites show promising magnetic properties in their undoped forms that originate from the presence of intrinsic vacancy defects.[26,28] It is, therefore, intuitive to examine the magnetism in BSO introduced by the presence of vacancy defects. On the other hand, the robustness of the Dirac cones against SOC may be exploited by controlled incorporation of intrinsic vacancy defects in BSO for tuning its electronic bands.[61] For the supercells of BSO with intrinsic vacancies, we first evaluate the thermodynamic stability of three possible charge-neutral vacancy defects (V^0_{Ba}, V^0_{Sn} and V^0_O) by computing the defect-formation energies. It is worth pointing out here that charged vacancy defects in perovskite-like materials exhibiting an insulating band structure are commonly studied to evaluate the relative stability of all possible vacancy defects. However, the semimetallic nature of the electronic band structure shown in Fig. 3 clearly suggests that BSO is unlikely to possess charged vacancy defects.[70] In the present study, we computed the defect-formation energies, $E^f[Z^0]$, of charge-neutral vacancies (Z = Ba, Sn or O) using the relation[75]

$$E^f[Z^0] = E_{tot}[Z^0] - E_t[B_3SnO] + \mu_Z \quad (15)$$

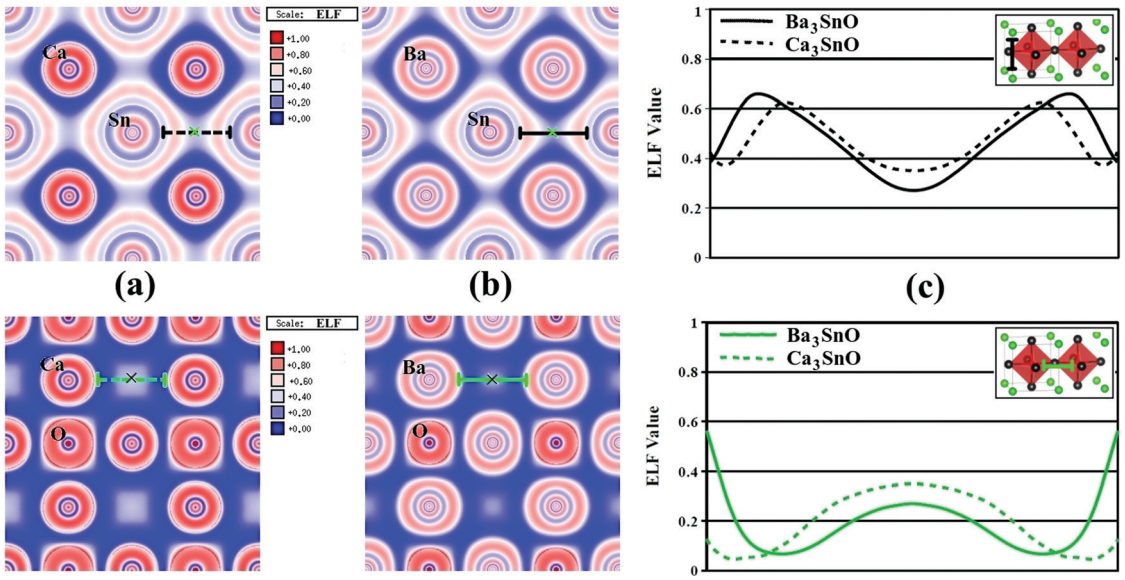

Fig. 4 Comparison of the electronic localization functions (ELFs) corresponding to AB layer (top panels) and A_2O layer (bottom panels) in pristine (a) Ca_3SnO and (b) Ba_3SnO. (c) Shows the ELF profiles of the metallic interaction between the Sn atoms in Ca_3SnO (dashed lines) and Ba_3SnO (solid lines), which are evaluated along the black and green lines indicted in (a) and (b). The relationship between the black and green lines used for ELF profiling can be understood from the crosses in (a) and (b) or the lines shown in the insets of (c).

where $E_{tot}[Z^0]$ and $E_t[B_3SnO]$ are the minimum total energies of a BSO supercell with a charge-neutral vacancy and pristine BSO, respectively. The last term in eqn (15), $\mu_Z = (\mu_Z^{solid/gas} + \Delta\mu_Z)$, represents the atomic chemical potential of the vacancy atom Z, which varies according to points A, B, C, D and X within the thermodynamic stability region of BSO displayed in Fig. 1. Since the incorporation of vacancy defects in BSO can lead to a magnetic state, we first determine the energetically stable (*i.e.*, $\Delta E = E_{NSP} - E_{SP}$) electronic structure of supercells of BSO with a vacancy by performing spin-polarized (SP) and non-spin-polarized (NSP) calculations. For all the vacancy defect cases considered here, the energetically stable system is subsequently used for obtaining $E_{tot}[Z^0]$ in eqn (15). From Table 3 it is evident that for the supercells containing V_{Ba}^0 and V_{Sn}^0, $E_{tot}[Z^0]$ can be set equal to both E_{NSP} and $E_{tot}[Z^0]$ because an energy difference in the range of ± 1 meV per atom between SP and NSP calculations is insignificant compared with the precision of modern DFT codes and has a negligible influence on the formation energies discussed here.[49] On the other hand, Table 3 clearly shows that $E_{tot}[Z^0] = E_{SP}$ for the case of a BSO supercell with V_O^0. It is worth mentioning here that the physics governing the emergence of magnetism in d^0 compounds is complex compared with conventional magnetism in transition metal- and rare-earth-based systems. In the backdrop of the debates concerning the origin of magnetism in undoped d^0 systems such as $LaAlO_3/SrTiO_3$, ZrO_2 and SnO_2,[71–74] the past decade has seen a number of studies confirming the emergence of ferromagnetism in A_3BO anti-perovskite materials.[26–29] For instance, a recent study by Arras *et al.*[29] has shown that vacancy concentration and ordering have a significant impact on the stability of ferromagnetism in undoped anti-perovskites SSO. It is, therefore, important to examine the influence of oxygen-vacancy ordering on the ferromagnetism in BSO. In the present study, we also simulated an oxygen vacancy inside a $3 \times 3 \times 3$ supercell of BSO, which corresponds to a 3.704% vacancy concentration. The reason for using $2 \times 2 \times 2$ and $3 \times 3 \times 3$ supercells in the present work is that they allow an ordered distribution of oxygen vacancies to be tested and avoid disordered distribution (*e.g.*, in the $2 \times 2 \times 3$ supercell), which requires low-symmetry crystal structures. Our results confirm the persistence of ferromagnetism in oxygen-deficient BSO as the distance between two V_O^0 vacancies increases from 11.018 Å in the $2 \times 2 \times 2$ supercell to 16.527 Å in the $3 \times 3 \times 3$ supercell. In addition to confirming the ordered distribution of oxygen vacancies in BSO, we also examined the influence of magnetic ordering of the O vacancy

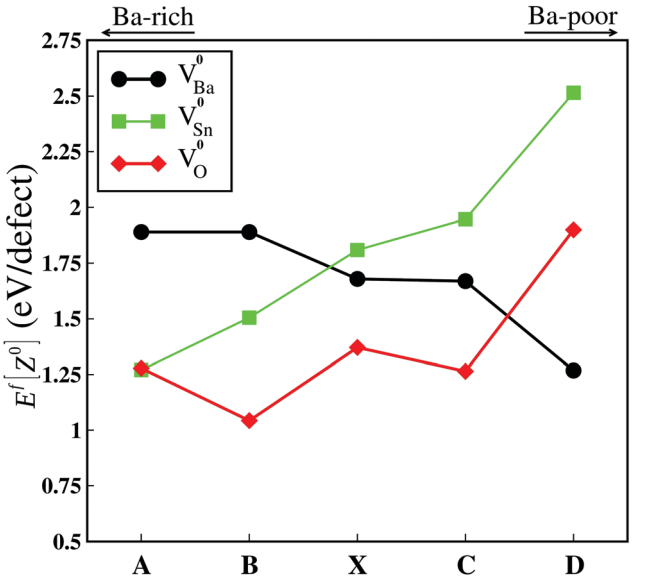

Fig. 5 Calculated defect-formation energies of neutral intrinsic vacancies V_{Ba}^0, V_{Sn}^0 and V_O^0 in Ba_3SnO at the points defined in Fig. 1.

sites in BSO by computing the energy difference between ferromagnetic (SP) ordering and anti-ferromagnetic ordering. This is done by considering two oxygen-vacancy-containing $2 \times 2 \times 2$ supercells of BSO stacked along the [001] direction such that the magnetic moments at the V_O^0 site may be aligned parallel or anti-parallel to each other.[33] The calculated energy difference between parallel (E_{SP}) and anti-parallel ($E_{SP\text{-}AFM}$) ordering is found to be 163.361 meV, which shows that parallel alignment of the magnetic moments is energetically stable compared with both NSP and anti-ferromagnetic order. This robustness of ferromagnetism in O-vacancy-containing BSO can be ascribed to the larger band overlap in this system compared with CSO and SSO.

Fig. 5 displays the calculated defect-formation energies for V_{Ba}^0, V_{Sn}^0 and V_O^0 vacancies in BSO at the stability points shown in Fig. 1. For points A and B, both V_{Sn}^0 and V_O^0 have low defect-formation energies, indicating the stability of anion-vacancy defects in BSO under Ba-rich growth conditions. Although both Sn and O vacancies are equally likely to exist in BSO at point A, Fig. 5 clearly shows that charge-neutral oxygen vacancies having $E^f[O^0] = 1.043$ eV per defect are the most dominant form of point defect in BSO at point B. The thermodynamically favourable situation for V_O^0 in BSO also persists for points X and C;

Table 3 Relative changes (in %) in the 1st and 2nd NN distances between Ba-, Sn- and O-vacancy-containing $2 \times 2 \times 2$ supercells of Ba_3SnO with respect to the NN distances in the pristine unit cell. The atomic species NN to the vacancy site are indicated inside the parentheses. The energy differences between spin-polarized and non-spin-polarized calculations, ΔE (meV), and the total and interstitial magnetic moments (in μ_B) inside the supercell computed using spin-polarized calculations are also shown

Vacancy in Ba_3SnO	Relative change in the NN distance from vacancy site (in %)		Energy difference $\Delta E = E_{NSP} - E_{SP}$	Total (interstitial) magnetic moment MM_T (MM_I)
	1st NN	2nd NN		
V_{Ba}	5.66 (O × 2)	−5.96 (Ba × 4), 3.72 (Sn × 8)	−0.42	0.00 (0.00)
V_{Sn}	2.62 (Ba × 12)	−0.44 (O × 8)	−0.200	0.00 (0.00)
V_O	5.56 (Ba × 6)	−0.40 (Sn × 8)	163.44	1.10 (0.91)

however, V_{Ba}^{0} is the most thermodynamically stable form of vacancy defect in the O-rich/Ba-poor chemical environment. A comparison of all the calculated defect-formation energies in Fig. 5 indicates that V_{Ba}^{0} and V_{O}^{0} are likely to exist in BSO for a wide range of its chemical stability compared with V_{Sn}^{0}. However, at the nominal chemical environment (point X) for obtaining BSO without the precipitation of any of its competing phases, V_{O}^{0} has a defect formation energy that is still $\sim$0.3 eV per defect less than the defect-formation energy of V_{Ba}^{0}. Since SP simulations for the O-vacancy-containing supercell of BSO lead to the most energetically stable electronic structure, it is evident that the increased likelihood of V_{O}^{0} to occur at point X is due to the exchange energy.

3.5. Structural, magnetic and binding properties of vacancy-defect-containing Ba_3SnO

In the pristine unit cell of BSO, the GGA-optimized distance between a Ba atom and its two 1st nearest neighbour (NN) O atoms is 2.754 Å. On the other hand, four Ba and eight Sn atoms form 2nd NN positions to a Ba atom, which are all located 3.895 Å away. For the case of the Sn atom, twelve Ba atoms and eight O atoms are 1st and 2nd NNs that are located at distances of 3.895 Å and 4.771 Å, respectively. From the above, it is clear that six Ba atoms are coordinated octahedrally with each O atom located at a distance of 2.754 Å, while eight Sn atoms located 4.771 Å away are 2nd NNs to each O atom. As soon as an intrinsic vacancy defect is introduced in BSO, the atoms surrounding the vacancy site are displaced from their ideal atomic positions in the anti-perovskite lattice to compensate for the missing ion. After geometry optimization, we computed the relative changes (in %) in the 1st and 2nd NN atoms of vacancy sites in BSO with respect to their pristine limits, which are presented in Table 3. It is evident that the 1st NN atoms move away from the vacancy site in all cases, while the 2nd NN atoms are drawn closer to the vacancy site. However, for the case of the 2nd NN Sn atoms of a vacant Ba site one can see a displacement towards the vacancy site owing to the opposite charge states of Ba and Sn in pristine BSO. It is also interesting to note from Table 3 that the displacement of O and Ba atoms, respectively, near V_{Ba} and V_{O} is larger compared with the displacement of the Ba atoms near V_{Sn}, indicating stronger ionic binding between Ba and O.

Comparing the results of SP and NSP simulations, we find that geometry optimization leads to similar atomic positions. This can be attributed to the fact that repositioning of the atomic species surrounding a vacancy site is mainly influenced by the elimination of Coulomb interactions. This is also evident from the outward (inward) movement of the 1st (2nd) NN atoms having a charge state that is opposite to the charge state of the vacant atomic site. However, spin-polarization shows a noticeable influence on the calculated total energy in the V_{O}^{0}-containing supercell of BSO. Owing to the above-mentioned reasons, the magnetic properties, electron localization functions (ELFs) and electronic properties of all the BSO supercells with vacancies were computed using SP simulations along with SOC. The energetic stability of the SP simulations for the BSO supercells with V_{O}^{0} can be attributed to the unpaired electronic charges at the vacancy site and contributions from Ba-5d due to repopulation of the charge previously donated to O, which give a net magnetic moment of 1.10 μ_B. For the case of the Sn vacancy, on the other hand, no net magnetic moment is obtained in the SP simulations. From Table 3 it is evident that the energetically stable magnetism in the BSO supercell with V_{O}^{0} is mainly caused by the magnetic moment in the interstitial region. In order to identify the origin of this large interstitial magnetic moment, we compare the relative changes in the Bader charges of the atomic species surrounding the vacancy sites, as given in Table 4. For the case of O and Sn vacancies, the Bader charges for nearby Ba atoms are found to be 1.017 *e* and 1.129 *e*, respectively. Since the Bader charge of the 1st NN Ba atom of a vacant O site is significantly smaller (*i.e.*, a large negative value in Table 4) compared with its bulk value, it is clear that the missing O in the BSO supercell results in unpaired electronic charge in the interstitial region between the Ba atoms and the vacant O site. Since the electronic charges shared by a Ba atom with its surrounding anions have 5d character, the local repopulation of these states due to the introduction of oxygen vacancies results in occupation of spin-up Ba-5d states, which gives rise to a net magnetic moment.

To understand the differences in the redistribution of charges in the Ba-5d states upon creation of Sn and O vacancies, we computed their ELFs, which are presented in Fig. 6. In addition, the spin-dependent charge-density profiles at the vacancy site for the selected paths are also shown in Fig. 6, which allow us to identify the charge contribution for the ELF at the vacancy sites. It is worth pointing out here that the Sn–V_{Ba}^{0}–Sn, Sn–V_{Sn}^{0}–Sn and Ba–V_{O}^{0}–Ba paths for spin-dependent charge-density profiles are selected based on the fact that the largest relative changes in the Bader charges are observed for Sn, Sn and Ba atoms, respectively, in Table 4. Since a Ba atom is the 1st NN to both Sn and O atoms, the introduction of V_{Ba}^{0} in the BSO supercell causes the ELFs to change in both the BaSn and Ba_2O layers. It is clear from Fig. 6(a) that the ELFs of both Sn and O atoms near a Ba vacancy are modified compared with the ELFs of the BaSn and Ba_2O layers of pristine BSO (Fig. 4(b)). Interestingly, introducing V_{Ba}^{0} in BSO causes a large reduction in the metallic interaction among the Sn atoms. This is in complete conformity with the large relative decrease (−6.78%) of the Bader charge for a Sn atom located near the Ba vacancy site (Table 4). However, one can see that there is no difference between the spin-up and spin-down charge-density profiles at

Table 4 Relative changes (in %) in the Bader charges of the atoms located near the Ba, Sn and O vacancy sites in 2 × 2 × 2 supercells of Ba_3SnO with respect to the Bader charges of the same atomic species in a pristine unit cell

	Relative change in the Bader charge (in %)		
Vacancy in Ba_3SnO	Ba	Sn	O
V_{Ba}	0.27	−6.78	−1.08
V_{Sn}	1.48	2.97	0.27
V_{O}	−11.26	0.41	−0.86

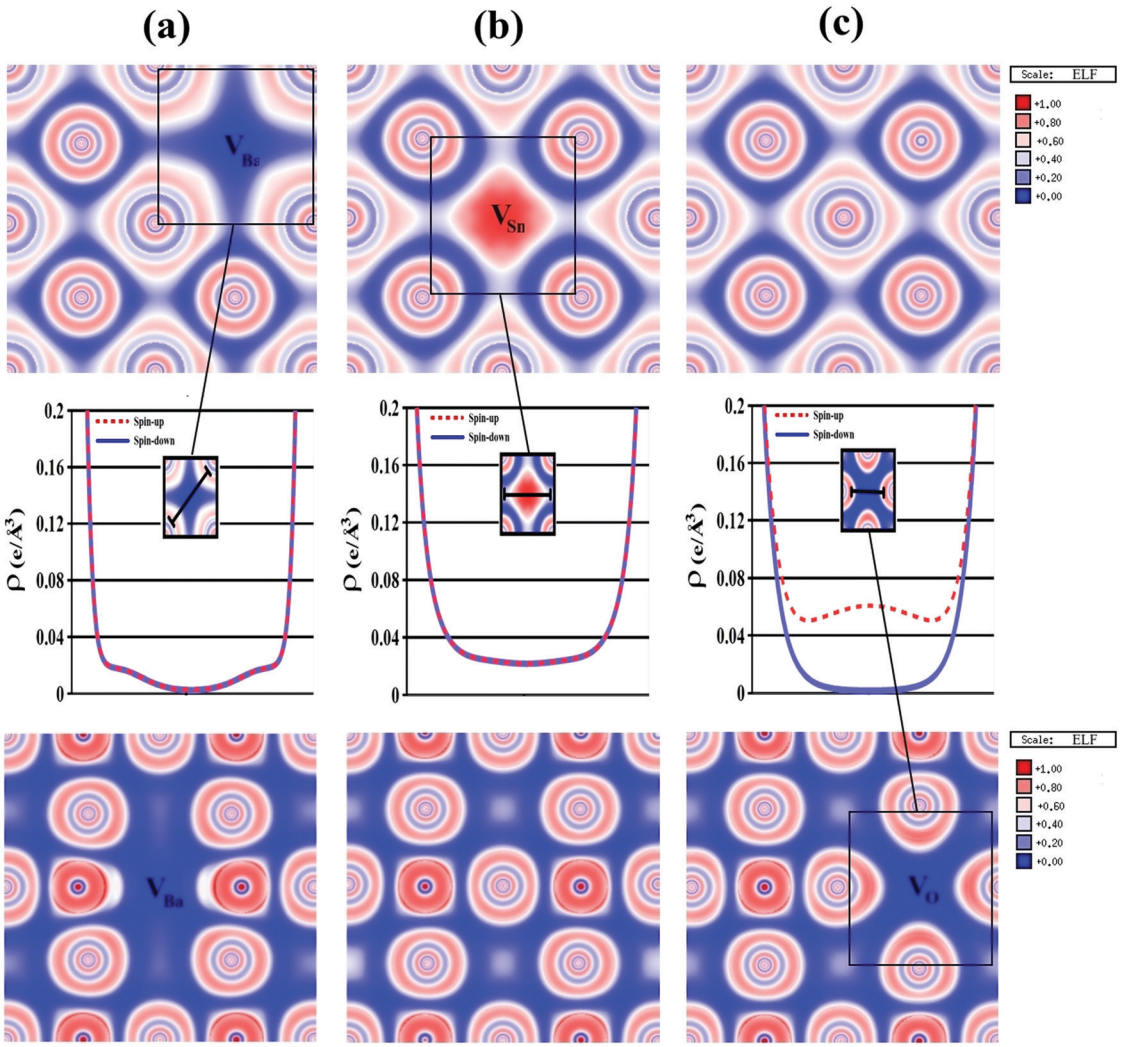

Fig. 6 Electronic localization functions (ELFs) corresponding to BaSn layers (top panels) and Ba_2O layers (bottom panels) of (a) V^0_{Ba}-, (b) V^0_{Sn}- and (c) V^0_O-vacancy-containing supercells of Ba_3SnO. The spin-dependent charge-density profiles (middle panel) along the Sn–V^0_{Ba}–Sn, Sn–V^0_{Sn}–Sn and Ba–V^0_O–Ba paths for Ba, Sn and O vacancies, respectively.

the V^0_{Ba} site, in accordance with the non-magnetic behaviour of this vacancy defect.

Contrary to the case of the V^0_{Ba}-containing BSO, changes in the ELF for V^0_{Sn} or V^0_O in BSO are only prominent inside the BaSn or Ba_2O layer, respectively. When a charge-neutral V^0_{Sn} is introduced in BSO, a large ELF value (*i.e.*, ~1) at the Sn vacancy site of the BaSn layer (Fig. 6(b)) is obtained along with slight elongation of Ba atom's ELF towards the vacancy site. Since an equal contribution for the spin-up and spin-down charge densities is evident from the charge-density profile at the V^0_{Sn} site (Fig. 6(b)), it is clear that the large ELF is mainly caused by the charges contributed by the Sn and Ba atoms (see Table 4). From Fig. 6(c), it can be seen that introducing V^0_O in BSO results in a low ELF value (*i.e.*, ~0) at the vacant O site, together with larger protrusions in the ELF of the Ba atoms towards the vacancy. Since an ELF value of ~0 can indicate the presence of unpaired electrons, it is clear that the introduction of V^0_O in BSO results in the accumulation of charges between Ba atoms surrounding the vacancy site. As Table 4 clearly shows that the largest relative change in the Bader charge for a V^0_O vacancy is achieved for the nearby Ba atoms, comparison of the spin-dependent charge-density profiles along the Ba–V^0_O–Ba paths confirms the unpaired spin-up charge in the region between the Ba atoms. This is in accordance with the large contribution of the interstitial magnetic moment to the net magnetic moment, which results in a magnetic ground state for an isolated V^0_O-containing BSO. Our analysis unequivocally shows that the Ba vacancy has no electron density, while the O vacancy accepts one electron and the Sn vacancy accepts two electrons. We attribute these donations of electrons to the vacancy to the fact that it is favorable for the neighboring Ba atoms to lose these electrons and keep their ionic nature and binding as in pristine BSO. It also indicates that the largest change in the Ba Bader charge is for the O vacancy (see Table 4).

3.6. Electronic properties of vacancy defects in Ba_3SnO

To understand the influence of the isolated intrinsic vacancy defects on the electronic properties of BSO, we compare the

electronic density of states for the vacancy-containing supercells in Fig. 7. The TDOS clearly shows that only the introduction of a Ba vacancy causes the electronic bands that are mainly composed of Sn-5p states to shift above the Fermi level. Moreover, in the two spin channels shown in Fig. 7(b) one can see a similar nature in the spin-up and spin-down channels. For the case of the Sn vacancy, on the other hand, the unoccupied Ba-5d states of pristine BSO become partially occupied and are relocated below the Fermi level. Compared with bulk BSO, it is interesting to note that both the Sn-5p and Ba-6d states equally dominate the DOS around −0.5 eV for a V_{Sn}^{0}-containing supercell of BSO. In addition, the Ba-5d states appearing below the Fermi level are seen to be separated from the main bulk-like conduction bands. This is contrary to the case of tin vacancies in Ca_3SnO[28] and can mainly be attributed to the fact that BSO has a larger band overlap compared with other members of this anti-perovskite family.[12] This, together with the increase of the Bader charges (Table 4) for Ba and Sn atoms near the tin vacancy, clearly suggests that equal amounts of spin-up and spin-down charges are contributed by a strong mixture of 5p and 5d states of neighboring Sn and Ba atoms of a Sn vacancy site.

From Fig. 7(e and f), it is evident that the electronic density of states for the two spin channels of a V_{O}^{0}-containing supercell of BSO are different. A close inspection of the PDOS plots shown in Fig. 7(f) shows that Ba-5d and O-2p states contribute almost equally in the spin-up channel of the valence band. These contributions are in stark contrast with the PDOS plots of pristine BSO shown in Fig. 3 where only the Sn-5p contribution is dominant. On the other hand, the contribution of Ba-5d states in the same energy region of PDOS is slightly reduced in the spin-down channel and shows no significant contribution coming from the O-2p states. It is also clear from Fig. 7(f) that there is a noticeable difference of the contribution of the Ba-5d state for both spin-up and spin-down channels that are located below the Fermi level. In addition, the contribution of O-2p states in the conduction band is found to be shifted closer to the Fermi level in the spin-down channel. Since the contributions of Ba-5d states and O-2p states above the Fermi level are also spin-polarized, it can be inferred that the electronic charge responsible for the interstitial magnetic moment near V_{O}^{0} in BSO also causes the depletion of charges from the oxygen atoms bound with these Ba atoms. The difference in the PDOS plots of Fig. 7(f) are in agreement with the calculated changes in the Bader charges (Table 4) discussed above, which showed that introducing V_{O}^{0} in BSO causes the Ba atom to retain some of its charge with 5d character in the vacancy region that appears as a highly non-spherical ELF with large lobes pointing towards the vacancy site (see Fig. 6(c)). Referring back to Table 4, one can see that the oxygen atoms neighboring the Ba atoms around the V_{O}^{0} also show small changes in their Bader charges. In order to see how these affect the introduced magnetism we computed the 3D spin-density isosurface (Fig. 8(a)) and the Ba_2O layer 2D spin density (Fig. 8(b)) of V_{O}^{0}-containing BSO. It is clear that the spin-polarization is mainly located in the region between the Ba atoms in the oxygen-vacancy site. Moreover, Fig. 8(a) shows an opposite spin density at the nearest oxygen sites. The major contribution to

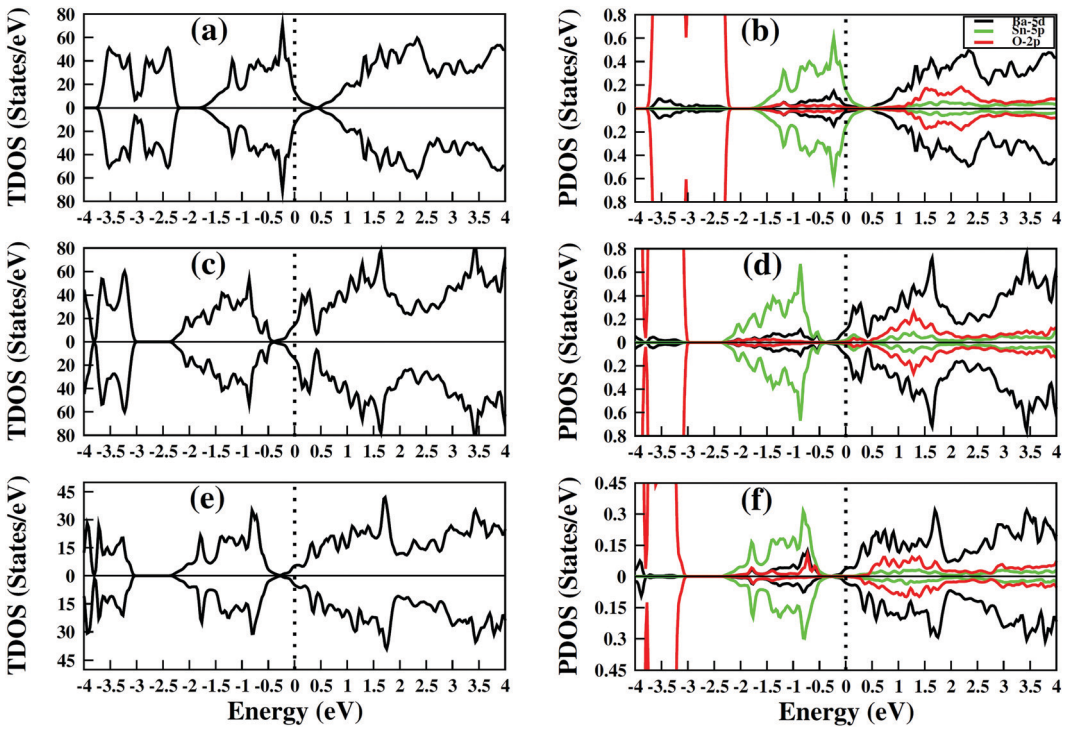

Fig. 7 Total and partial electronic density of states (DOS) for Ba- (a and b), Sn- (c and d) and O-vacancy-containing (e and f) supercells of BSO for spin-up (top panel) and spin-down (bottom panel) channels. The Fermi level is set at 0 eV and is represented by the dashed line.

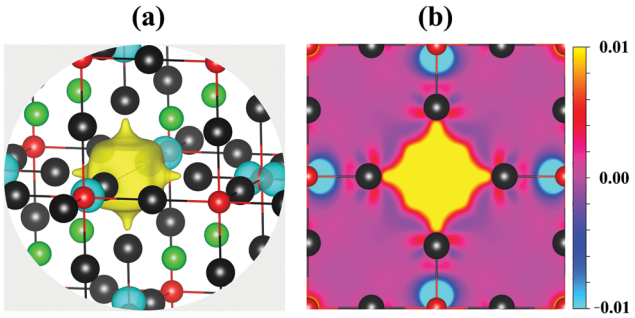

Fig. 8 (a) 3D spin-density isosurfaces for a V_O^0-containing supercell of Ba_3SnO. Ba, Sn and O atoms are represented by black, green and red spheres, respectively. The accumulation and depletion of electrons are represented by yellow and turquoise regions, respectively. (b) 2D spin-density plot corresponding to the V_O^0-containing Ba_2O layers shown in (a). For both (a) and (b) the spin-density differences in the range from -0.01 e Å^{-3} to $+0.01$ e Å^{-3} are displayed.

the total magnetic moment of V_O^0-containing BSO coming from the interstitial region is also confirmed. Since our calculated defect-formation energies (Fig. 5) clearly indicate V_O^0 to be the dominant form of intrinsic vacancy defect in BSO, it is clear that magnetism in this semimetal can be experimentally induced by controlling the oxygen-vacancy concentration.[27] Moreover, manipulation of the Dirac cones in the vicinity of the Fermi level may be realized through intentional incorporation of intrinsic vacancy defects under various growth conditions (*i.e.*, Ba-rich and Ba-poor) owing to their strong robustness against SOC caused by the large band overlap in BSO.[12,61]

4. Conclusions

In this study, the thermodynamic stability of pristine and intrinsic vacancy-defect-containing topological Dirac semimetal BSO is studied using all-electron density functional theory calculations. The calculated thermodynamic properties indicate that BSO can be synthesized with respect to its competing binary phases Ba_2Sn, BaSn and BaO under a predominantly barium-dominated chemical environment. The electronic band structure of pristine BSO is found to be influenced by spin–orbit coupling and displays semimetallic character consisting of twin Dirac cones along the Γ–X direction below the Fermi level. In order to elucidate the factors responsible for the emergence of the Dirac semimetal phase in BSO, we make use of the electronic density of states, effective Bader charges and electron localization function. We show that the contribution of the Ba-5d and Sn-5p states in the valence and conduction bands, respectively, is inverted in the vicinity of the Fermi level. Compared with the electronic structure of Ca_3SnO – a 3D topological insulator – the ELF and effective Bader charges computed for bulk BSO indicate that a smaller metallic interaction between two Sn atoms in a BaSn layer results in significant contribution of the Sn-5p states above the Fermi level. Consequently, a larger band overlap is achieved in BSO, which is responsible for giving this quantum material a semimetallic band structure. Motivated by the observation of ferromagnetism in the undoped 3D topological insulator Sr_3SnO in earlier experimental studies,[26,27] we systematically examined the possibility of realizing a magnetic state in undoped TDS BSO by means of introducing charge-neutral intrinsic vacancy defects in a supercell configuration. Using valid limits of the atomic chemical potentials derived from the thermodynamic stability diagram, we compared the relative stability of Ba, Sn and O vacancy defects in BSO. The calculated defect formation energies clearly show that charge-neutral oxygen vacancies are the most favourable type of vacancy defect in BSO. Moreover, our calculations show that spin-polarized calculations with a parallel alignment of spins for the oxygen vacancy in BSO give the most energetically stable system. Our analysis has revealed that among the three formally neutral isolated intrinsic vacancies in BSO, only V_{Ba}^0 results in a vacancy site without electron density. On the other hand, O- and Sn-vacancy-containing BSO receive electronic charges from the surrounding Ba atoms. However, only O-vacancy-containing BSO is found to be magnetic, while Sn-vacancy-containing BSO is non-magnetic. Our results show that the magnetism in V_O^0-containing BSO originates from the accumulation of spin-up electrons at the oxygen vacancy sites that are strongly coupled with the 5d states of the neighboring Ba atoms. Since earlier theoretically predicted magnetic TDSs have been found to show structural metastability and/or complex magnetic ordering in experiments, magnetism in BSO originating from the presence of isolated oxygen-vacancy defects could prove useful in realizing magnetic TDSs for future technological applications.

Author contributions

Javaria Batool: conceptualization, data curation, and writing – original draft. Syed Muhammad Alay-e-Abbas: conceptualization, data curation, validation, and writing – original draft. Gustav Johansson: formal analysis, writing – review and editing and validation. Waqas Zulfiqar: validation and visualization. Muhammad Arsam Danish: formal analysis and validation. Muhammad Bilal: formal analysis and validation. J. Andreas Larsson: conceptualization, writing – review and editing, formal analysis and supervision. Nasir Amin: conceptualization, writing – review and editing and supervision.

Conflicts of interest

There are no conflicts to declare.

Acknowledgements

J. B. would like to acknowledge the in-house GRG project GCWUF/GRG/ST/16/15. S. M. A. A. and J. A. L. thank the Knut and Alice Wallenberg Foundation, and Kempestiftelserna for financial support. The authors are grateful to the Higher Education Commission of Pakistan for financial support under the National Research Program for Universities grant no. 7107/Punjab/NRPU/R&D/HEC/2017. The computations were enabled

by resources provided by the Swedish National Infrastructure for Computing (SNIC) at HPC2N and NSC, partially funded by the Swedish Research Council through grant agreement no. 2018-05973.

References

1 J. Zou, Z. He and G. Xu, *npj Comput. Mater.*, 2019, **5**, 96.
2 A. K. Geim and K. S. Novoselov, *Nat. Mater.*, 2007, **6**, 183–191.
3 L. D. Landau, *Zh. Eksp. Teor. Fiz.*, 1936, **7**, 19–32.
4 J. Hu, S.-Y. Xu, N. Ni and Z. Mao, *Annu. Rev. Mater. Res.*, 2019, **49**, 207–252.
5 F. Wilczek, *Phys. Today*, 1998, **51**, 11–13.
6 M. Z. Hasan and C. L. Kane, *Rev. Mod. Phys.*, 2010, **82**, 3045.
7 N. P. Armitage, E. J. Mele and A. Vishwanath, *Rev. Mod. Phys.*, 2018, **90**, 015001.
8 A. Bernevig, H. Weng, Z. Fang and X. Dai, *J. Phys. Soc. Jpn.*, 2018, **87**, 041001.
9 P. J. W. Moll, N. L. Nair, T. Helm, A. C. Potter, I. Kimchi, A. Vishwanath and J. G. Analytis, *Nature*, 2016, **535**, 266–270.
10 T. Liang, Q. Gibson, M. N. Ali, M. Liu, R. J. Cava and N. P. Ong, *Nat. Mater.*, 2015, **1**, 280–284.
11 T. Kariyado and M. Ogata, *J. Phys. Soc. Jpn.*, 2011, **80**, 083704.
12 T. Kariyado and M. Ogata, *Phys. Rev. Mater.*, 2017, **1**, 061201.
13 A. Widera and H. Schafer, *Mater. Res. Bull.*, 1980, **15**, 1805–1809.
14 T. Zhou, C. Zhang, H. Zhang, F. Xiu and Z. Yang, *Inorg. Chem. Front.*, 2016, **3**, 16371643.
15 Z. Wang, H. Weng, Q. Wu, X. Dai and Z. Fang, *Phys. Rev. B: Condens. Matter Mater. Phys.*, 2013, **88**, 125427.
16 Z. K. Liu, B. Zhou, Y. Zhang, Z. J. Wang, H. M. Weng, D. Prabhakaran, S.-K. Mo, Z. X. Shen, Z. Fang, X. Dai, Z. Hussain and Y. L. Chen, *Science*, 2014, **343**, 864–867.
17 N. Sivadas, S. Okamoto and D. Xiao, *Phys. Rev. Lett.*, 2016, **117**, 267203.
18 R. Cheng, S. Okamoto and D. Xiao, *Phys. Rev. Lett.*, 2016, **117**, 217202.
19 N. Sivadas, M. W. Daniels, R. H. Swendsen, S. Okamoto and D. Xiao, *Phys. Rev. B: Condens. Matter Mater. Phys.*, 2015, **91**, 235425.
20 B. L. Chittari, Y. Park, D. Lee, M. Han, A. H. MacDonald, E. Hwang and J. Jung, *Phys. Rev. B*, 2016, **94**, 184428.
21 M.-W. Lin, H. L. Zhuang, J. Yan, T. Z. Ward, A. A. Puretzky, C. M. Rouleau, Z. Gai, L. Liang, V. Meunier, B. G. Sumpter, P. Ganesh, P. R. C. Kent, D. B. Geohegan, D. G. Mandrus and K. Xiao, *J. Mater. Chem. C*, 2016, **4**, 315–322.
22 C. Gong, L. Li, Z. Li, H. Ji, A. Stern, Y. Xia, T. Cao, W. Bao, C. Wang, Y. Wang, Z. Q. Qiu, R. J. Cava, S. G. Louie, J. Xia and X. Zhang, *Nature*, 2017, **546**, 265–269.
23 P. Tang, Q. Zhou, G. Xu and S.-C. Zhang, *Nat. Phys.*, 2016, **12**, 1100–1104.
24 K. Kim, J. Seo, E. Lee, K.-T. Ko, B. S. Kim, B. G. Jang, J. M. Ok, J. Lee, Y. J. Jo, W. Kang, J. H. Shim, C. Kim, H. W. Yeom, B. I. Min, B.-J. Yang and J. S. Kim, *Nat. Mater.*, 2018, **17**, 794–799.
25 S. Nie, H. Weng and F. B. Prinz, *Phys. Rev. B*, 2019, **99**, 035125.
26 Y. F. Lee, F. Wu, R. Kumar, F. Hunte, J. Schwartz and J. Narayan, *Appl. Phys. Lett.*, 2013, **103**, 112101.
27 Y. F. Lee, J. Narayan and J. Schwatz, *MRS Commun.*, 2014, **4**, 7–13.
28 J. Batool, S. M. Alay-e-Abbas and N. Amin, *J. Appl. Phys.*, 2018, **123**, 161516.
29 R. Arras, J. Gosteau, D. Huang, H. Nakamura, H. J. Zhao, C. Paillard and L. Bellaiche, *Phys. Rev. B*, 2021, **104**, 045411.
30 D. Mishra, B. P. Mandal, R. Mukherjee, R. Naik, G. Lawes and B. Nadgorny, *Appl. Phys. Lett.*, 2013, **102**, 182404.
31 D. Kim, J. Hong, Y. R. Park and K. J. Kim, *J. Phys.: Condens. Matter*, 2009, **21**, 195405.
32 P. Esquinazi, W. Hergert, D. Spemann, A. Setzer and A. Ernst, *IEEE Trans. Magn.*, 2013, **49**, 4668–4674.
33 P. Blaha, K. Schwarz, G. Madsew, D. Kvasnicka and J. Luitz. *WIEN2k: An Augmented Plane Wave Plus Local Orbital Program*, Vienna University of Technology, Austeria, 2014.
34 J. P. Perdew, K. Burke and M. Ernzerhof, *Phys. Rev. Lett.*, 1997, **78**, 1396.
35 A. D. Becke and K. E. Edgecombe, *J. Chem. Phys.*, 1990, **92**, 5397–5403.
36 F. D. Murnaghan, *Proc. Natl. Acad. Sci. U. S. A.*, 1944, **30**, 244–247.
37 J. Nuss, C. Mühle, K. Hayama, V. Abdolazimi and H. Takagi, *Acta Crystallogr., Sect. B: Struct. Sci., Cryst. Eng. Mater.*, 2015, **71**, 300–312.
38 A. S. Bhalla, R. Guo and R. Roy, *Mater. Res. Innov.*, 2000, **4**, 3–26.
39 S. M. Alay-e-Abbas, S. Nazir, S. Cottenier and A. Shaukat, *Sci. Rep.*, 2017, **7**, 8439.
40 A. Jain, S. P. Ong, G. Hautier, W. Chen, W. D. Richards, S. Dacek, S. Cholia, D. Gunter, D. Skinner, G. Ceder and K. A. Persson, *APL Mater.*, 2013, **1**, 011002.
41 W. Xing, H. Sha, F. Meng and R. Yu, *J. Mater. Chem. C*, 2021, **9**, 6324–6331.
42 F. Tran, R. Laskowski, P. Blaha and K. Schwarz, *Phys. Rev. B: Condens. Matter Mater. Phys.*, 2007, **75**, 115131.
43 K. Guttsche, A. Rosin, M. Wendorff and C. Röhr, *Z. Naturforsch. B*, 2006, **61**, 846–853.
44 F. Merlo and M. L. Fornasini, *J. Less Common Met.*, 1967, **13**, 603–610.
45 R. B. Elo, S. P. Murarka and R. A. Swalin, *J. Phys. Chem. Solids*, 1973, **34**, 97–106.
46 M. J. Mehl and D. A. Papaconstantopoulos, *Phys. Rev. B: Condens. Matter Mater. Phys.*, 1996, **54**, 4519–4530.
47 S. Q. Wang and H. Q. Ye, *Phys. Rev. B: Condens. Matter Mater. Phys.*, 2002, **66**, 235111.
48 D. W. Oxtoby, H. Pat Gillis and A. Campion, *Principles of Modern Chemistry*, 7th edn, Cengage Learning, Massachusetts, USA, 2011.
49 K. Lejaeghere, V. Van Speybroeck, G. Van Oost and S. Cottenier, *Crit. Rev. Solid State Mater. Sci.*, 2014, **39**, 1–24.
50 T. Lichtenstein, J. Gesualdi, C.-T. Yu and H. Kim, *J. Alloys Compd.*, 2019, **811**, 151531.

51 O. Kubaschewski and H. Villa, *Ztschr. Elektrochem*, 2019, **53**, 32–40.
52 V. S. Sudavtsova, L. O. Romanova, V. G. Kudin, M. I. Ivanov and A. S. Kozorezov, *Powder Metall. Met. Ceram.*, 2020, **59**, 445–453.
53 M. W. Chase Jr., NIST-JANAF Thermochemical Tables, 4th edn, *J. Phys. Chem. Ref. Data*, 1998, **4**, 9.
54 C. Kittel, *Introduction to Solid State Physics*, 8th edn, John Wiley & Sons Inc., USA, 2005.
55 P. Canepa, S.-H. Bo, G. S. Gautam, B. Key, W. D. Richards, T. Shi, Y. Tian, Y. Wang, J. Li and G. Ceder, *Nat. Commun.*, 2017, **8**, 1759.
56 S. B. Zhang and J. E. Northup, *Phys. Rev. Lett.*, 1991, **67**, 2339–2342.
57 P. Erthart and K. Albe, *J. Appl. Phys.*, 2007, **102**, 084111.
58 J. Vidal, X. Zhang, L. Yu, J.-W. Lou and A. Zunger, *Phys. Rev. B: Condens. Matter Mater. Phys.*, 2011, **84**, 041109(R).
59 I. Barin, *Thermochemical Data of Pure Substances*, 3rd edn, John Wiley & Sons Inc., USA, 1995.
60 T. H. Hsieh, J. Liu and L. Fu, *Phys. Rev. B: Condens. Matter Mater. Phys.*, 2014, **90**, 081112(R).
61 S. Lei, S. M. L. Teicher, A. Topp, K. Cai, J. Lin, G. Cheng, T. H. Salters, F. Rodolakis, J. L. McChesney, S. Lapidus, N. Yao, M. Krivenkov, D. Marchenko, A. Varykhalov, C. R. Ast, R. Car, J. Cano, M. G. Vergniory, N. P. Ong and L. M. Schoop, *Adv. Mater.*, 2021, 2101591, DOI: 10.1002/adma.202101591.
62 M. Ochi and K. Kuroki, *Phys. Rev. Appl.*, 2019, **12**, 034009.
63 T. Zhang, Y. Jiang, Z. Song, H. Huang, Y. He, Z. Fang, H. Weng and C. Fang, *Nature*, 2019, **566**, 475–479.
64 R. F. W. Bader, *Acc. Chem. Res.*, 1985, **18**, 9–15.
65 M. Setvin, M. Reticcioli, F. Poelzleitner, J. Hulva, M. Schmid, L. A. Boatner, C. Franchini and U. Diebold, *Science*, 2018, **359**, 572.
66 S. Thiel, G. Hammerl, A. Schmehl, C. W. Schneider and J. Mannhart, *Science*, 2006, **313**, 1942.
67 A. Palenzona, P. Manfrinetti and M. L. Fornasini, *J. Alloys Compd.*, 2000, **312**, 165.
68 K. Koumpouras and J. A. Larsson, *J. Phys.: Condens. Matter*, 2020, **32**, 315502.
69 A. Savin, *J. Mol. Struct.*, 2005, **727**, 127.
70 H.-P. Komsa, N. Berseneva, A. V. Krasheninnikov and R. M. Nieminen, *Phys. Rev. X*, 2014, **4**, 031044.
71 A. Brinkman, M. Huijben, M. van Zalk, J. Huijben, U. Zeitler, J. C. Maan, W. G. van der Wiel, G. Rijnders, D. H. A. Blank and H. Hilgenkamp, *Nat. Mater.*, 2007, **6**, 493.
72 N. H. Hong, J. Sakai, N. Poirot and V. Brizé, *Phys. Rev. B: Condens. Matter Mater. Phys.*, 2006, **73**, 132404.
73 G. Bouzerar and T. Ziman, *Phys. Rev. Lett.*, 2006, **96**, 207602.
74 N. H. Hong, N. Poirot and J. Sakai, *Phys. Rev. B: Condens. Matter Mater. Phys.*, 2008, **77**, 033205.
75 J. L. Lyons and C. G. Van de Walle, *npj Comput. Mater.*, 2017, **3**, 12.